



저작자표시-비영리-변경금지 2.0 대한민국

이용자는 아래의 조건을 따르는 경우에 한하여 자유롭게

- 이 저작물을 복제, 배포, 전송, 전시, 공연 및 방송할 수 있습니다.

다음과 같은 조건을 따라야 합니다:



저작자표시. 귀하는 원저작자를 표시하여야 합니다.



비영리. 귀하는 이 저작물을 영리 목적으로 이용할 수 없습니다.



변경금지. 귀하는 이 저작물을 개작, 변형 또는 가공할 수 없습니다.

- 귀하는, 이 저작물의 재이용이나 배포의 경우, 이 저작물에 적용된 이용허락조건을 명확하게 나타내어야 합니다.
- 저작권자로부터 별도의 허가를 받으면 이러한 조건들은 적용되지 않습니다.

저작권법에 따른 이용자의 권리는 위의 내용에 의하여 영향을 받지 않습니다.

이것은 [이용허락규약\(Legal Code\)](#)을 이해하기 쉽게 요약한 것입니다.

[Disclaimer](#)

Thesis for the Degree of Master of Engineering

**Novel Diffusing Optical Fiber:  
Fabrication and Applications for  
Photothermal Therapy**



by

Trung-Hau Nguyen

Department of Biomedical Engineering

The Graduate School

Pukyong National University

August 2015

# **Novel Diffusing Optical Fiber: Fabrication and Applications for Photothermal Therapy**

Advisor: Prof. Hyun Wook Kang

by  
Trung-Hau Nguyen

A thesis submitted in partial fulfillment of the requirements  
for the degree of

Master of Science

In Department of Biomedical Engineering, The Graduate School,  
Pukyong National University

August 2015

**Novel Diffusing Optical Fiber: Fabrication and Applications  
for Photothermal Therapy**

A dissertation  
by  
Trung Hau Nguyen

Approved by:



Prof. Jung Hwan Oh, Ph.D. (Chairman)



Prof. Hyun Wook Kang, Ph.D. (Member)



Prof. Seung Yun NAM, Ph.D. (Member)

August 2015

# **Novel Diffusing Optical Fiber: Fabrication and Applications for Photothermal Therapy**

**Trung-Hau Nguyen**

**Department of Biomedical Engineering, Graduate School,  
Pukyong National University**

## **Abstract**

Photo-thermal therapies has limited efficacy and application due to difficulties in propagating light inside tissue especially in human body. Optical flat fiber recently was used as a feasible tool to deliver laser energy to targeted tissue. In this study, we introduce a novel optical fiber which was micro-machined from a 600  $\mu\text{m}$  flat fiber to achieve the laterally uniform light distribution. Uniform pattern was engraved on the fiber surface using focused CO<sub>2</sub> laser beam at 5 W. Spatial emission of the fiber tip was visualized to validate the performance of the fabricated diffuser. For spatial characteristics, polar, azimuthal, and longitudinal emissions were evaluated. The spatial emission characteristics of diffusing fiber presented an almost uniform power distribution along the diffuser tip and around its circumference. Visible light distribution and egg-white test demonstrated a well agreement with the spatial emission characteristics. A computational model was also developed to predict spatio-temporal heat distribution during interstitial laser coagulation. Both simulation and tissue testing demonstrated approximately 1-*mm* coagulation thickness at 6 W for 10 *sec* with 1470 *nm*. A diffuser protected by glass-cap combined with near-infrared wavelength (1470 *nm*) was used to thermally decompose urethral stricture tissue structure. By providing direct delivery of diffuse light to the target tissue while minimizing undesirable photo-thermal damage in the adjacent tissue, the proposed optical diffuser may be a feasible tool to treat the tubular tissue structures in a uniform and circumferential manner.

## Table of Contents

<b>Abstract</b> .....	<b>iv</b>
<b>Table of Contents</b> .....	<b>v</b>
<b>List of Figures</b> .....	<b>vii</b>
<b>List of Figures</b> .....	<b>x</b>
<b>List of Abbreviations</b> .....	<b>xi</b>
<b>I. INTRODUCTION</b> .....	<b>1</b>
1. Laser-tissue Interaction .....	1
1.1. Optical effect .....	2
1.2. Thermal effect.....	4
2. Optical fiber .....	7
3. Urethral Stricture.....	8
4. Research Objective .....	9
<b>II. MATERIALS AND METHODS</b> .....	<b>13</b>
1. Fabrication Process .....	13
2. Experiment Setup for Spatial Emission Measurements .....	16
3. Numerical Simulation Model: Comparison between Flat and Diffusing fiber.....	17
3.1. Geometry .....	17
4. Experiment Setup for Tissue Test with Fabricated Diffuser.....	21
5. Experiment Setup for Urethral Tissue Irradiation.....	22
<b>III. RESULTS</b> .....	<b>24</b>
1. SEM and Visible Light Emission images of Diffuser tip .....	24
2. Spatial Emission from Diffuser tip .....	27

3. Simulation Results .....	28
4. Tissue Test Results.....	34
5. In Vitro Experiment Result.....	35
<b>IV. DISCUSSION .....</b>	<b>37</b>
<b>V. CONCLUSION.....</b>	<b>41</b>
<b>VI. FUTHER STUDIES.....</b>	<b>42</b>
<b>References .....</b>	<b>44</b>
<b>Acknowledgments .....</b>	<b>46</b>



## List of Figures

<b>Figure 1.</b> Spatial distribution of thermal effect following laser vaporization of tissue.....	1
<b>Figure 2.</b> Absorption coefficient spectra for various tissue constituents .....	3
<b>Figure 3.</b> Light intensity propagation in tissue based on Monte Carlo simulation.....	4
<b>Figure 4.</b> Summary of physics phenomenon in thermal interactions of light with tissue .....	6
<b>Figure 5.</b> Principle of light propagation in an optical fiber based on internal reflection .....	7
<b>Figure 6.</b> Demonstration of a typical diffusing optical fiber.....	10
<b>Figure 7.</b> An example of applications of an optical fiber-based laser ( $\lambda = 1064\text{ nm}$ ) in phototherapy-based tumor treatment .....	10
<b>Figure 8.</b> Diagram of fiber machining set-up for optical diffuser using CO <sub>2</sub> laser (H: fiber holder, T: translational stage, and R: rotational stage) .....	14
<b>Figure 9.</b> Entire of optical fiber micro-machining system .....	15
<b>Figure 10.</b> Schematic illustration of Goniometric measurements. (a) Polar emission measurement setup. (b) Azimuthal and longitudinal emission measurement setup. Note a dash-dot line represents an axis of rotation for a photodiode.....	17
<b>Figure 11.</b> Geometry of numerical simulation model of fiber-based laser-tissue interaction. (a) flat-tip fiber 0.6 mm diameter application. (b) 10 mm long, 0.6 mm diameter diffusing fiber application. Note that both flat-tip and diffusing fiber were protected by a .....	17

**Figure 12.** Comparison of spatial emission between a flat-tip fiber and a diffusing fiber. Note that diffusing fiber with 10 mm long was tapered..... 24

**Figure 13.** Images of optical diffuser fabricated at 45°. (a) SEM image (15 kV, ×250) of fiber surface. (b) HeNe light distribution from fiber tip (P: proximal and D: distal ends)..... 25

**Figure 14.** SEM images comparison between two diffusing fibers with different fabricated parameter. (a) 5 W CO<sub>2</sub> laser with short interaction time. (b) 6 W CO<sub>2</sub> laser with longer interaction time. Note that above images was ×100 magnification SEM and below image was ..... 26

**Figure 15.** Demonstration of intensity comparison between two diffusing fiber: with and without tapering process..... 27

**Figure 16.** Normalized light intensity from 10 mm long diffusing fiber. (a) Polar emission. (b) Azimuthal emission. (c) Longitudinal emission..... 28

**Figure 17.** Spatial temperature distribution. (a) Temperature development at the tissue interface within 15 sec irradiation time at three power levels: 3, 6, and 9 W. (b) Longitudinal view of temperature distribution from diffuser tip after 10-sec, 6 W. (c) Longitudinal view of temperature distribution from flat-tip fiber after 10-sec, 6 W..... 29

**Figure 18.** Thermal effect of 10-sec photocoagulation of diffuser. (a) Cross-sectional view of temperature distribution from diffuser tip. (b) Cross-sectional view of corresponding thermal damage with log<sub>10</sub> of Arrhenius integral ..... 30

**Figure 19.** Thermal effect of 10-sec photocoagulation of flat-tip fiber. (a) Cross-sectional view of temperature distribution from incident region of laser beam. (b) Cross-sectional view of corresponding thermal damage with log<sub>10</sub> of Arrhenius integral ..... 31

<b>Figure 20.</b> Spatial temperature distribution compared between flat-tip fiber and diffusing fiber in numerical simulation. (a) Along longitudinal distance. (b) In radial distance .....	32
<b>Figure 21.</b> Egg-white coagulation test with 5-W, 1470-nm laser for 120-sec irradiation time. (a) Before irradiation. (b) After irradiation. And (c) Temperature development as a function of time at three power level 2, 3, and 4 W .....	34
<b>Figure 22.</b> Effect of laser power on tissue coagulation with optical diffuser. (a) Temporal evolution of tissue coagulation at 6 W with 1470 nm (P: proximal and D: distal ends; bar = 5 mm). (b) Variations in coagulation depths as function of time for three different power levels ( $N = 5$ ) .....	35
<b>Figure 23.</b> H&E-stained histological images of urethral tissue treated for 10 sec at 6 W with 1470 nm. (a) Gross image ( $\times 12.5$ ; bar = 2 mm). (b) Magnified image of transition zone ( $\times 100$ ; bar = 200 $\mu\text{m}$ ) .....	36
<b>Figure 24.</b> Balloon catheter-based diffusing fiber. (a) Principle of the combined technique between balloon and diffuser. (b) Real image of the device including an inflator.....	42

## List of Tables

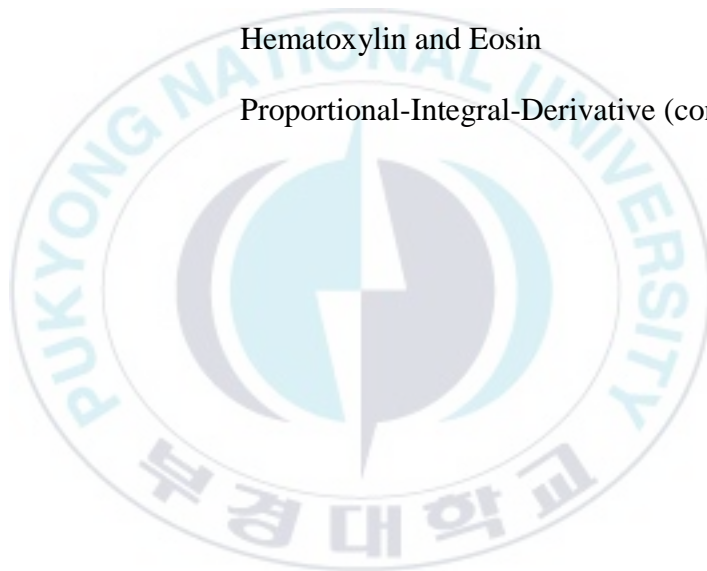
**Table 1.** Thermal properties of materials used in simulation model

**Table 2.** Physical parameters of liver tissue used for thermal damage model



## List of Abbreviations

Laser	Light Amplification by Stimulated Emission of Radiation
SEM	Scanning Electron Microscope
3D	Three Dimensions
NA	Numerical Aperture
UV	Ultra-violet
H&E	Hematoxylin and Eosin
PID	Proportional-Integral-Derivative (controller)



# I. INTRODUCTION

## 1. Laser-tissue Interaction

There are many different mechanisms happened when laser light interacts with tissue. The most common interaction mechanisms for therapeutic and surgical applications can be divided into five broad classes: photochemical reactions, photothermal interactions, photoablation, plasma-induced photoablation, and photodisruption [1]. Among these classes, thermal effects are the most widely applied for tissue-laser interaction in clinical practice.

With photothermal effects, photons will be absorbed by biomolecule that leads to a thermal effect. Depend on the temperature level and exposure time, there are four different tissue regions surrounding laser beam incident region due to either hyperthermia, coagulation, carbonization, or vaporization effects.

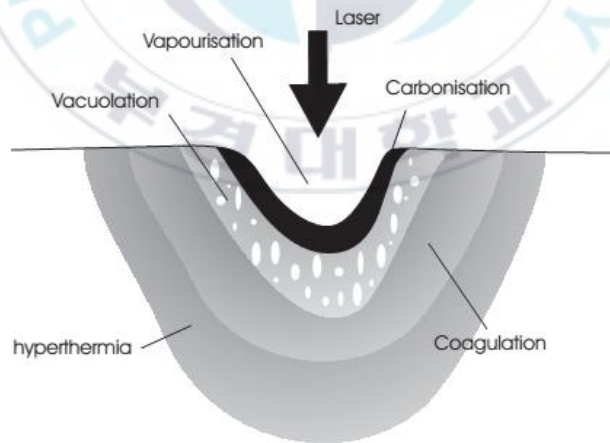


**Figure 1.** Spatial distribution of thermal effect following laser vaporization of tissue

## 1.1. Optical effect

Light propagation in tissue was primarily governed by Beer's law which light intensity was exponentially decreased along tissue depth:

$$I(z) = I_0 e^{-\mu_a z} \quad (1)$$

where  $I(z)$  ( $W/cm^2$ ) is light intensity at the tissue depth of  $z$ ,  $I_0$  is incident light intensity, and  $\mu_a$  is absorption coefficient of the light in tissue. The absorption coefficient  $\mu_a$  of a tissue is the sum of contributions from all absorbing chromophores within the tissue:

$$\mu_a = \ln(10) \sum_i C_i \varepsilon_i \quad (2)$$

where  $C$  is the concentration ( $mol \cdot L^{-1}$ ), and  $\varepsilon$  is the extinction coefficient ( $cm^{-1} M^{-1}$ ) for the chromophore. Since the molecular composition of the tissue is not well specified, tissue properties will usually cite values of a tissue's average absorption coefficient  $\mu_a$ . So that the equation (2) can be rewritten using the volume fraction of a tissue component ( $f_{v,i}$  ( $L \cdot L^{-1}$ )) and the absorption coefficient of that pure component ( $\mu_{a,i}$  ( $cm^{-1}$ )):

$$\mu_a = \sum_i f_{v,i} \mu_{a,i} \quad (3)$$

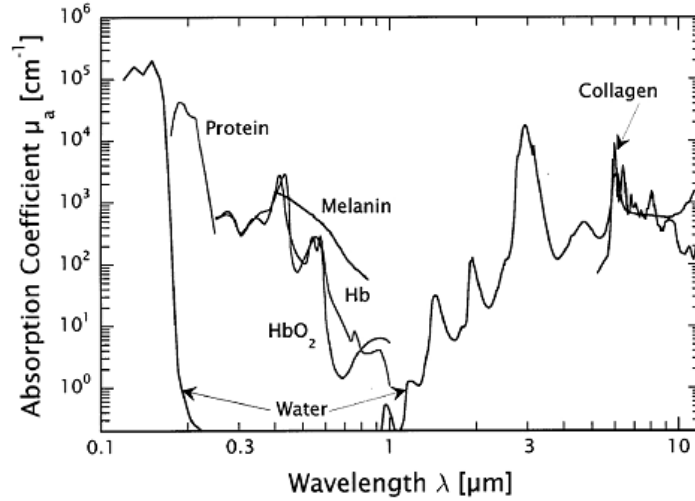


**Figure 2.** Absorption coefficient spectra for various tissue constituents

The photon propagation in the tissue could be simulated based on Monte Carlo simulation to track the travelling paths of photons. Figure 3 demonstrates an example of numerical simulation based on Monte Carlo method. This simulation called Monte Carlo XYZ which has the ability to map 3D distribution of Fluence and Energy Deposition in biological tissue.

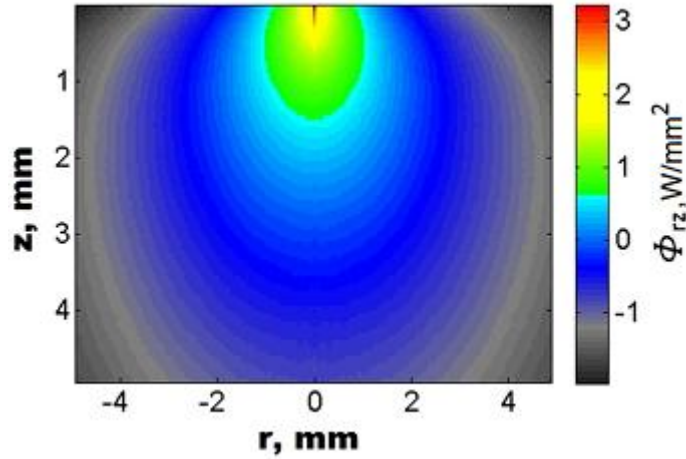


**Figure 3.** Light intensity propagation in tissue based on Monte Carlo simulation

## 1.2. Thermal effect

Absorbed optical energy which depends on tissue properties (absorption and scattering coefficient) induced heat source. Deposited heat energy will diffuse through the tissue due to thermal conductivity effect, causing a rise in temperature in surrounding tissue. The rise in temperature leads to thermal damage to the tissue. As well as thermal conduction, heat can be transferred by radiation and convection when blood flow or perfusion through tissues is significant. In general, heat transfer in tissue can be described by bio-heat equation called Pennes equation:

$$\rho C \frac{\partial T}{\partial t} + \nabla(-k\nabla T) = \rho_b C_b \omega_b (T_b - T) + Q_{met} + Q_{ext} \quad (4)$$

where  $\rho$  ( $kg/m^3$ ),  $c$  ( $J/kg \cdot K$ ), and  $k$  ( $W/m \cdot K$ ) are density, specific heat, and thermal conductivity of the liver tissue respectively,  $T$  ( $K$ ) the local tissue temperature, and  $Q_{ext}$  ( $W/m^3$ ) the heat source associated with light absorption.

Since neither metabolic heat generation nor blood perfusion was considered in the current model owing to in vitro experiments, (4) can be simplified as:

$$\rho c_p \frac{\partial T}{\partial t} = \frac{1}{r} \frac{\partial}{\partial r} \left( kr \frac{\partial T}{\partial r} \right) + \frac{\partial}{\partial z} \left( k \frac{\partial T}{\partial z} \right) + Q_{ext} \quad (5)$$

Thermal damage of cells and tissue was described by a first-order thermal-chemical rate equation, which represents the rate when molecules become thermally denatured or [1]:

$$\Omega(r, t) = A_f \int_0^t \exp\left(\frac{-E_a}{R \cdot T(r, t)}\right) dt \quad (6)$$

where  $A_f$  (1/s) is the frequency factor,  $E_a$  (J/mol) the denaturation activation energy,  $R$  (J/mol·K) the universal gas constant of 8.314,  $T$ (K) the absolute temperature in tissue, and  $\Omega$  the level of thermal damage.  $\Omega = 1$  represents the extent of irreversible thermal damage that occurs in 63% of tissue due to temperature increase up to approximately 338 K [1]. In general, summary of the laser-tissue interaction can be described by flow chart shown in Fig. 4.

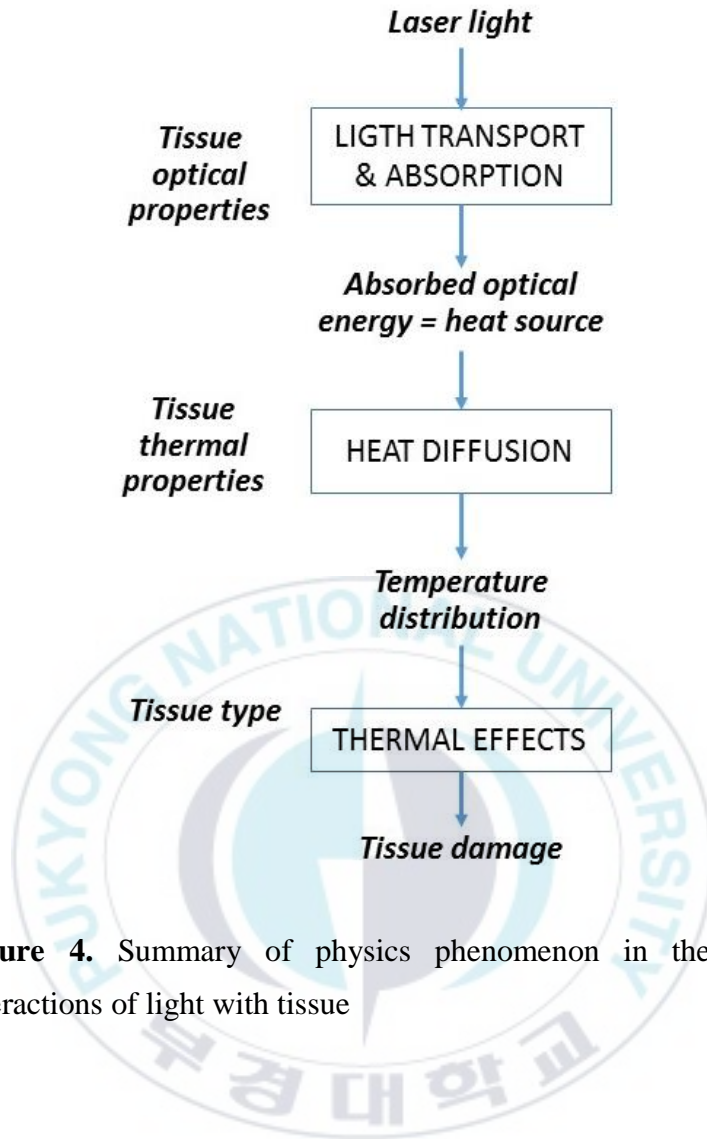


**Figure 4.** Summary of physics phenomenon in thermal interactions of light with tissue

## 2. Optical fiber

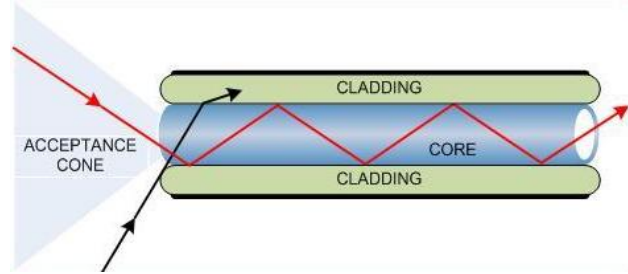


**Figure 5.** Principle of light propagation in an optical fiber based on internal reflection

Optical fibers are actual media that guides the light. They can be made of glass or plastic. A typical fiber is made up of a core, cladding, and a jacket. The core is the center where the light propagates. The cladding surrounds the core and has a refractive index lower than that of the core, in this way the light will propagate through the core by means of internal reflection. Surrounding the cladding is the jacket which serves to protect the entire optical fiber. The most important is to consider the characteristics involved when coupling a light source to a fiber. Light gathering ability of the fiber is called numerical aperture ( $NA$ ). A large  $NA$  means a larger signal, or ray loss, and larger distortion. The  $NA$  can be represented by the following Equation:

$$NA = \sqrt{n_1^2 - n_2^2} \quad (7)$$

$$NA = \sin \theta$$

where  $n_1$  is the index of core and  $n_2$  is the index of the cladding.  $\theta$  is the half-angle of the acceptance cone of the fiber.

### 3. Urethral Stricture

Urethral stricture is scarring of urethral pathway involving a fibrotic process of spongy erectile tissue (i.e. corpus spongiosum) [2]. The corpus spongiosum lies under urethral epithelium, of which fibrosis and contraction often lead to scarring and eventual reduction in a urethral luminal diameter (i.e. spongiofibrosis). According to the data from Veterans Affairs (VA) in 2003, a prevalence rate of the urethral stricture was estimated to be 0.2% (i.e. 193 per 100,000 diagnoses) in US [3]. Among the diagnosed population, approximately 20% of patients develop symptomatic strictures due to iatrogenic causes such as traumatic catheterization, penile inflammation, congenital disease, and urological injuries to genitourinary tract [4]. The patients with the urethral strictures typically experience obstructive voiding symptoms including weak urinary stream, hematuria, pain, incomplete bladder emptying, and burning urinary infection [4]. Depending on characteristics of the stricture (i.e. location, etiology, size, and density of spongiofibrosis), several invasive treatments have been performed [5]. For instance, dilation with balloon or catheter is a temporary treatment that stretches fibrotic tissue to widen the urethral lumen [4]. Stent is another mid-term treatment option that places a small tube in a urethra to keep the stricture open. Urethrotomy is a surgical procedure performed under anesthesia that involves incision of the urethral to relieve the stricture. However, these treatment techniques have demonstrated high complication and recurrence rates associated with local pain, discomfort, and stone formation due to incomplete removal of the scarring tissue [4].

#### **4. Research Objective**

Lasers have been used for a variety of medical applications such as tissue ablation, blood coagulation, surgical resection, and optical imaging [6-10]. Due to short optical penetration depth associated with absorption and scattering events, non-invasive applications of lasers have often been limited. Thus, optical fibers have been used instead to incise, coagulate, and vaporize the diseased tissues. In particular, for photothermal treatment of urethral strictures, a flat fiber in conjunction with a flexible cystoscope is typically inserted into a genital to internally cut the targeted scarring tissue [10]. However, since the flat-tip fiber transmits high intensity light in a forward direction, it can hardly achieve uniform light distribution in tissue, which may cause non-homogenous coagulation and even carbonization during the thermal treatment. In the current study, to compensate directional limitations of the fibers for treating tubular structure tissue, a diffusing optical fiber was designed and developed to radially transmit uniform laser energy with low power intensity to the urethral stricture. It was hypothesized that based upon photothermal interactions, a relatively wide range of temperature distribution and accumulation in the urethral tissue could induce coagulative necrosis to selectively treat the stricture with minimal thermal injury to underlying corpus spongiosum. Based on a bare fiber, a diffusing optical fiber was fabricated by machining surface of the fiber. Therefore, light can be radially emitted surrounding fiber tip compared to forward direction emission within numerical aperture angle of a flat-tip fiber (Fig.6).

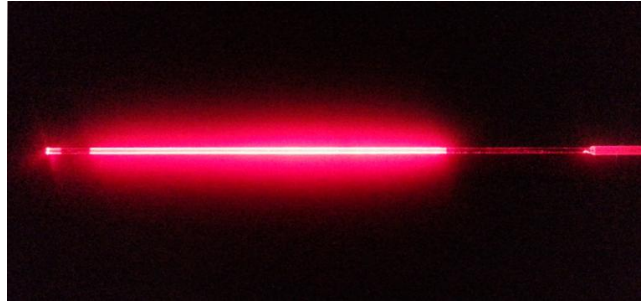


**Figure 6.** Demonstration of a typical diffusing optical fiber

Various biomedical applications of diffusing optical fibers have been investigated in the field of phototherapeutics such as photodynamic therapy, laser hair removal [11], laser lipolysis [12], and bladder carcinomas treatment [9]. Figure 7 showed a typical application of a diffusing optical fiber in tumor treatment. In this research, the diffuser covered by a transparent catheter was used to deliver laser energy (1060 nm) to the targeted tissue. Thermal effect leads to coagulated volume tissue surrounding diffuser.

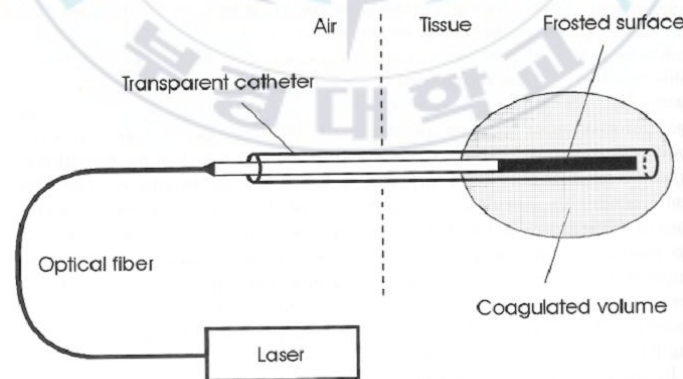


**Figure 7.** An example of applications of an optical fiber-based laser ( $\lambda = 1064 \text{ nm}$ ) in phototherapy-based tumor treatment

To fabricate the optical diffusers, a number of the manufacturing processes have been proposed; melt-drawing technique [13], acid-etching technique [12, 14], and UV micro-drilling technique [14]. For instance, micro-needles were fabricated for light diffusion by either melt-drawing or acid-etching techniques to have extremely a small diameter of shafts (33-125  $\mu\text{m}$ ) [12, 13]. Thus, the microneedles often suffered from mechanical weakness as well as limited fabrication length (i.e. shorter than 1  $\text{cm}$ ) [12, 13]. In the case of UV micro-drilling technique, the irradiance emitted from the diffuser presented a ripple profile due to gaps among multiple arrays of micro-holes on the fiber surface. In addition, the micro-holes in the diffuser induced low mechanical strength, leading to micro-cracking and variations in output intensity. Furthermore, the proposed fabrication techniques have accompanied multiple complex procedures that take a couple of hours [12, 14] to complete the fabrication process in a reliable manner. Additionally, the techniques were often difficult to control spatial emission profiles from the diffuser tip in terms of uniform light distribution and minimal forward propagation [12, 14].

In order to overcome the previous fabrication limitations, we developed a new technique to fabricate diffusing optical fibers by means of laser-assisted micromachining. For homogeneously circumferential light distribution with delivery of high power, a flat fiber was micro-machined by laser to engrave patterns on the fiber surface. The transmitted light could be diffused by means of varying the critical angles to reduce the probability of the total internal reflection inside the fiber. The fabricated fibers were evaluated in terms of optical imaging and goniometric measurements to characterize spatial

uniformity of light propagation. Spatio-temporal heat distribution in tissue firstly was modeled to estimate the degree of thermal coagulation for optimizing the treatment parameters during the interstitial irradiation. Then, in vitro tissue testing with a 1470-*nm* laser along with histological analysis was performed to construct thermal dosimetry to optimize the laser parameters for irreversible tissue coagulation.



## II. MATERIALS AND METHODS

### 1. Fabrication Process

Figure 8 presents a setup for laser micro-fabrication of an optical diffusing fiber. A 30-W CO<sub>2</sub> laser ( $\lambda=10.6 \mu\text{m}$ , Synrad, Mukilteo, WA, USA) was employed to deliver laser power for the fabrication process. Laser beam in a 3-mm diameter was expanded to approximately 7.5 mm by a combination of concave lens ( $f_1 = -25 \text{ mm}$ ) and convex lens ( $f_2 = 75 \text{ mm}$ ). Then, the expanded beam was focused on the fiber surface by another convex lens ( $f_3 = 25 \text{ mm}$ ). An air cooling system was also used to maintain clean surface at the machining area by removing any particles and melted parts. Multimode silica optical fibers with a 600- $\mu\text{m}$  in core diameter ( $NA = 0.48$ , Thorlab, Newton, New Jersey, USA) were used and fabricated for the current study. After removal of buffers with a mechanical stripper, an optical fiber was positioned in a fiber holder that was fixed at a motorized-stage system consisting of both translational and rotational stages (Fig. 1). To obtain helical groove patterns, the translational stage moved the fiber along the x-axis direction at the speed of 2~7 mm/s while the rotational stage was used to rotate the fiber at 240~480 rpm. Each movement speed was deliberately controlled and selected to avoid any overlapping between two consecutive grooves during the fabrication process. In turn, the fabrication angle between the fiber axis and the groove path was adjusted to be 45°, and the total length of the diffusing tip was 10 mm. All the motorized-stages were driven by a motion control system in conjunction with LabView software (National Instrument Corp., Austin, Texas, USA). Figure 8 shows entire of micromachining fabrication system of

optical fiber. Prior to every fabrication start, to reject the fluctuation error in laser power, a power meter was employed to measure the power of CO<sub>2</sub> laser to make sure it was correct value.

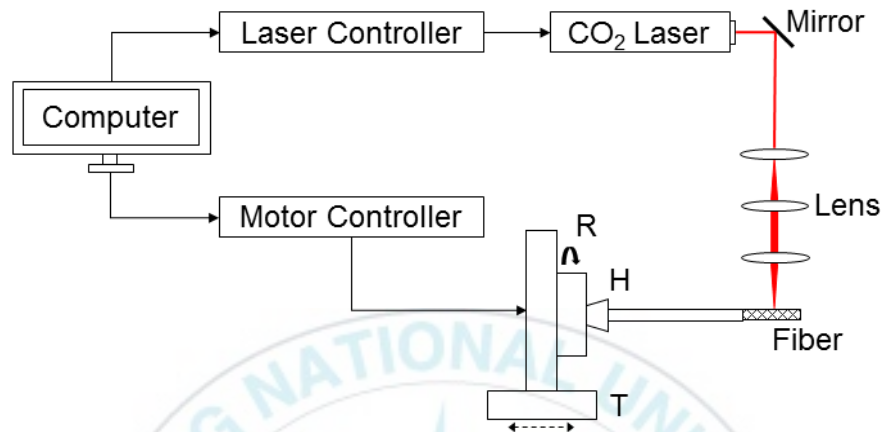


**Figure 8.** Diagram of fiber machining set-up for optical diffuser using CO<sub>2</sub> laser (H: fiber holder, T: translational stage, and R: rotational stage)

To validate the helical patterns induced by laser fabrication, the surface of the optical diffuser was imaged with scanning electron microscope (SEM). A HeNe ( $\lambda = 632 \text{ nm}$ , Thorlab, Newton, New Jersey, USA) laser was also employed to transmit laser light through the fabricated fiber and to roughly visualize the degree of light diffusion for swift evaluation on the fiber. The diffused light was imaged with a digital camera (D5100, Nikon Co., Ltd, Tokyo, Japan) in a dark room. To protect the fabricated part from any mechanical damage, the diffuser tip was covered with a glass cap (i.e., length =  $11 \text{ mm}$ , inner diameter =  $0.8 \text{ mm}$ , outer diameter =  $1.4 \text{ mm}$ , and thickness =  $0.2 \text{ mm}$ ) and sealed with epoxy.

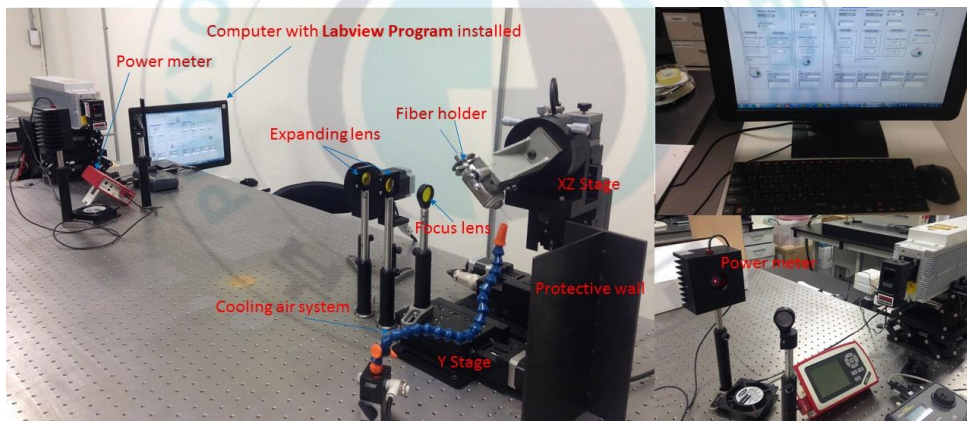


**Figure 9.** Entire of optical fiber micro-machining system

## 2. Experiment Setup for Spatial Emission Measurements

Spatial distribution of light intensity emitted from a fabricated diffuser tip was evaluated with a goniometric system, as shown in Fig. 10. The measurement set-up consisted of a photodiode head (PD-300-3W, Ophir, Jerusalem, Israel) and power meter (Nova II, Ophir, Jerusalem, Israel), based upon the methodology from Vesselov et al. [15]. A HeNe laser was used as a light source for the goniometric measurements. The photodiode with a sensing area of  $1 \text{ cm}^2$  and an acceptance angle of  $10^\circ$  was situated on a rotational rail platform with a radius of  $57 \text{ mm}$  to measure the power propagated from the fiber. For polar emission measurements, the diffuser was vertically positioned, and the photodiode sensor was rotated around the axis of the diffusing fiber at the middle point of the diffusing tip ( $5 \text{ mm}$  from distal end) in Fig. 10(a). Regarding azimuthal measurements, the sensor was rotated around the tip of the horizontally-located fiber, of which the axis of rotation was perpendicular to that of the fiber in Fig. 10(b). A step size for both the polar and the azimuthal measurements was  $10^\circ$ . Lastly, the sensor was moved by  $0.5 \text{ mm}$  along the fiber to measure longitudinal light emissions at various diffuser positions. The photodiode was positioned  $1 \text{ mm}$  above the diffuser, and a  $0.5 \times 0.5 \text{ mm}^2$  diaphragm slit was placed between the photodiode and the diffuser to prevent the detection of any diffusive light. All the measured intensities were normalized to minimize any power measurement errors.

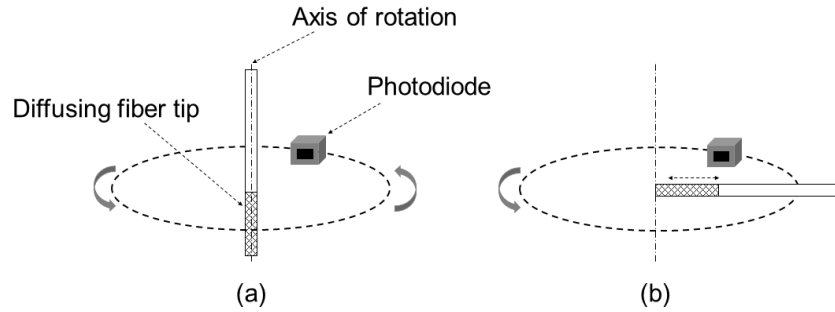


**Figure 10.** Schematic illustration of Goniometric measurements. (a) Polar emission measurement setup. (b) Azimuthal and longitudinal emission measurement setup. Note a dash-dot line represents an axis of rotation for a photodiode.

### 3. Numerical Simulation Model: Comparison between Flat and Diffusing fiber

#### 3.1. Geometry

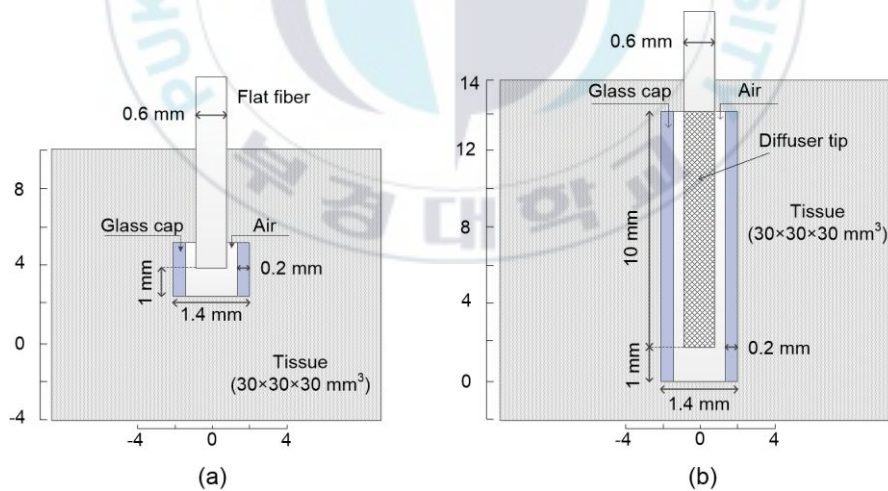


**Figure 11.** Geometry of numerical simulation model of fiber-based laser-tissue interaction. (a) flat-tip fiber 0.6 mm diameter application. (b) 10 mm long, 0.6 mm diameter diffusing fiber application. Note that both flat-tip and diffusing fiber were protected by a

Numerical simulations were conducted to estimate temperature distribution and the degree of thermal damage during laser coagulation, by using COMSOL finite-element-based software (v3.7, COMSOL Inc., Burlington, Massachusetts, USA). A model was based upon a glass-capped diffuser (11 mm long and 1.4 mm in outer diameter) that was inserted into a tissue specimen of 30×30×30 mm<sup>3</sup> (Fig. (11a)). In the case of flat-tip fiber model, the glass-capped diffuser was replaced by a glass-capped flat-tip fiber (2 mm long and 1.4 mm in outer diameter) in the model (Fig. (11b)). A 0.2-mm air gap exists between the fiber tip and the glass cap and 1-mm air gap exists between fiber end and the tissue. Bovine liver was used as a target tissue and irradiated by 1470-nm light at 3, 6, and 9 W. Thermal properties of the materials were considered independent of temperature and listed in Table 1. During the laser irradiation, heat transport within the tissue was described by using a bio-heat transfer equation as follows [16]:

$$\rho c_p \frac{\partial T}{\partial t} = \frac{1}{r} \frac{\partial}{\partial r} \left( kr \frac{\partial T}{\partial r} \right) + \frac{\partial}{\partial z} \left( k \frac{\partial T}{\partial z} \right) + Q_{ext} \quad (8)$$

where  $\rho$  (kg/m<sup>3</sup>),  $c$  (J/k·K), and  $k$  (W/m·K) are density, specific heat, and thermal conductivity of the liver tissue respectively,  $T$  (K) the local tissue temperature, and  $Q_{ext}$  (W/m<sup>3</sup>) the heat source associated with light absorption. Neither metabolic heat generation nor blood perfusion was considered in the current model owing to in vitro experiments. Due to application of a near-infrared wavelength of 1470 nm, no scattering effect was assumed, and light propagation in the liver was primarily governed by Beer's law [17]. In the diffuser-based model, the laser intensity was simplified to consist of two

directions of laser power, based upon goniometric measurements: radially emitted power from the diffusing part,  $P_1$  (assuming 80% of the incident laser power) and forward emitted power from the fiber tip,  $P_2$  (20% of the incident laser power). In turn, for the radial direction, the heat source was estimated as follows:

$$Q_{ext} = \frac{\mu_a P_1}{2\pi r l} e^{-\mu_a r} \quad (9)$$

where  $\mu_a$  ( $m^{-1}$ ) is the absorption coefficient of the tissue,  $r$  ( $m$ ) the radial distance from the diffuser surface, and  $l$  ( $m$ ) the diffuser length. The absorption coefficient of porcine liver tissue was  $19 \text{ cm}^{-1}$  [18]. For the forward direction, the light was diverged from the fiber tip ( $NA = 0.48$ ), and the spatial beam profile was assumed to be Gaussian. Thus, the heat source was a function of both the radial and the axial distances:

$$Q_{ext} = \frac{\mu_a P_2}{2\pi\sigma^2} e^{-\frac{r^2}{2\sigma^2}} \cdot e^{-\mu_a z} \quad (10)$$

where  $\sigma$  is the deviation of Gaussian distribution of the laser beam (i.e.,  $100 \mu m$  resulting from 99% of the output laser power in the fiber surface with a radius of  $300 \mu m$ ) and  $z$  ( $m$ ) the axial depth in tissue. In flat fiber-based model, there is only one heat source region which was resulted from the forward emission within numerical angle ( $NA = 0.48$ ) of the bare fiber. Furthermore, this heat source was estimated exactly same with the heat source for the forward direction in the diffuser-based model. The initial temperature was set to  $293 \text{ K}$ , and the external surface of the tissue was insulated (i.e.,  $\vec{n} \cdot \vec{k} \cdot \nabla T = 0$ , where  $\vec{n}$  is the direction of the heat flux).

**Table 1. Thermal properties of materials used in simulation model**

Material	$k$ (W/m·K)	$\rho$ (kg/m <sup>3</sup> )	$c$ (J/kg·K)	Reference
Glass	1.3	2200	820	[19]
Air	0.0257	1.205	1005	[19]
Liver tissue	0.513	1050	3600	[16]

Lastly, thermal damage of cells and tissue was described by a first-order thermal-chemical rate equation, which represents the rate when molecules become thermally denatured [1]. Damage was quantified by using a single parameter,  $\Omega$  that was calculated from the Arrhenius equation [1].  $\Omega$  is dimensionless, exponentially dependent on temperature and exposure time as followed:

$$\Omega(r, t) = A_f \int_0^\tau \exp\left(\frac{-E_a}{R \cdot T(r, t)}\right) dt \quad (12)$$

where  $A_f$  (1/s) is the frequency factor,  $E_a$  (J/mol) the denaturation activation energy,  $R$  (J/mol·K) the universal gas constant of 8.314,  $T$  (K) the absolute temperature in tissue, and  $\tau$  (sec) the duration of laser irradiation, which was 10 sec for the current damage model.  $\Omega = 1$  represents the extent of irreversible thermal damage that occurs in 63% of tissue due to temperature increase up to approximately 338 K [1]. All the physical properties of the liver are assumed to be constant during tissue coagulation and summarized in Table 2. Furthermore, the numerical simulation for flat fiber and diffusing fiber were conducted under same conditions and physical properties to see the different temperature distribution as well as the different tissue responses between them.

**Table 2. Physical parameters of liver tissue used for thermal damage model**

Parameter	Value	Reference
Absorption coefficient ( $\mu_a, cm^{-1}$ )	19	[18]
Scattering coefficient ( $\mu_s, cm^{-1}$ )	0	[18]
Frequency factor ( $A_f, 1/s$ )	$5.5 \times 10^{41}$	[1]
Activation energy ( $E_a, J/mol$ )	$2.77 \times 10^5$	[1]
Universal gas constant ( $R, J/mol \cdot K$ )	8.314	[1]

#### 4. Experiment Setup for Tissue Test with Fabricated Diffuser

In an attempt to determine thermal dosage for irreversible tissue denaturation, bovine liver tissue was tested with an optical diffuser in vitro. A 10-W 1470-nm laser system (Veincare, Wontech, Daejeon, Korea) was implemented as a light source for tissue testing. The liver tissue procured from a local abattoir was selected as a tissue model due to high light absorption features at 1470 nm ( $\mu_a = 19 cm^{-1}$ ) [18]. Each tissue specimen was prepared in size of  $3 \times 3 cm^2$  with flat surface and stored at 277 K prior to the tissue tests. For interstitial application of the optical diffuser, a 13-mm long cylindrical hole (1.4 mm in diameter) was initially created inside the tissue. Then, the glass-capped optical diffuser was inserted into the hole, and the 1470 nm laser light was interstitially and circumferentially irradiated to the liver tissue under various conditions. Three different power levels (3, 6, and 9 W) were implemented for in vitro tissue tests at various irradiation times from ablation threshold to 8 sec after the threshold with an increment of 2 sec (i.e., five data points in total). The ablation threshold was defined as the onset time of any evident discoloration on the tissue surface after laser irradiation at each power level. Each condition ran five times (N = 5) for the entire testing. Upon the

irradiation tests, each specimen was cross-sectioned along the axis of the optical diffuser, and the cross-sectional area was imaged with a portable microscope. Irreversible thermal denaturation was evaluated in light of any discoloration on the tissue surface. Coagulation depth was defined as the distance from the axis of the diffuser to the boundary of the discolored tissue region. Five measurements were conducted from the proximal to the distal end of the diffuser with Image J (National Institute of the Health, Bethesda, MD). For statistical analysis, Students' t-test were performed, and  $p < 0.05$  means significant.

## **5. Experiment Setup for Urethral Tissue Irradiation**

To explore the feasibility of transurethral treatment on urethral stricture, porcine urethral tissue (1.5 *cm* long and 1.5 *mm* in inner diameter) was experimented with a glass-capped optical diffuser in vitro. The urethral tissue was obtained from a local slaughter house and stored in isotonic saline at 277 *K* to prevent dehydration and structural deformation. Prior to coagulation tests, the diffuser was inserted through the urethral tissue, which was placed on a microscope slide in air. Due to the size of glass cap, the diffuser slightly made contact with the urethral wall. Based upon dosimetric studies with bovine tissue, the tissue was irradiated for 10 *sec* at 6 *W* with 1470-*nm* laser in order to achieve coagulation depth of approximately 1 *mm* ( $N = 3$ ). The average gross irradiance on the tissue surface was calculated to be approximately 12  $W/cm^2$ . Upon laser treatment, the tested tissue was fixed in 10% neutral-buffered formalin (VWR International, Westchester, PA) for five days and embedded in paraffin. Then, the treated region was sectioned into 4

$\mu\text{m}$  thick specimens and stained with hematoxylin and eosin (H&E). The prepared slides were imaged with an optical transmission microscope, and the extent of thermal denaturation was circumferentially measured around the urethral tissue ten times with Image J.



### III. RESULTS

#### 1. SEM and Visible Light Emission images of Diffuser tip

Figure 12 illustrates the difference of spatial emission profile between a flat-tip fiber and a diffusing optical fiber. The bare fiber emits 100% light energy in forward direction within numerical aperture angle ( $NA = 0.48$ ) while diffusing fiber radially emits light energy in lateral direction (around 80% of energy) (Fig. 12(b)). Almost 20% of energy was emitted in forward direction resulting in lower intensity compared to a flat-tip fiber (Fig. 12(a)).

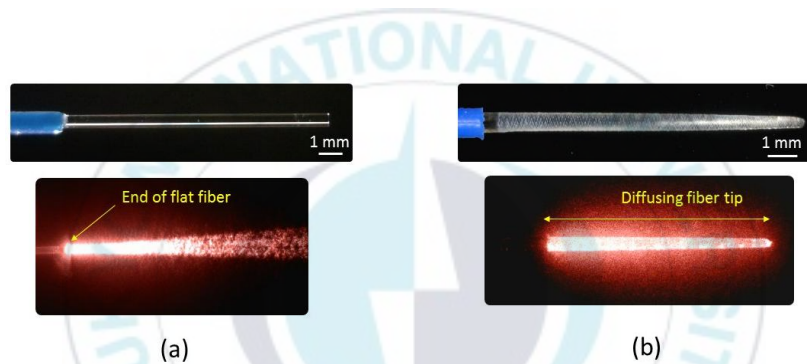


**Figure 12.** Comparison of spatial emission between a flat-tip fiber and a diffusing fiber. Note that diffusing fiber with 10 mm long was tapered

Figure 13(a) demonstrates a SEM image of the fiber surface fabricated at  $45^\circ$  with a  $\text{CO}_2$  laser. The image showed uniform helical groove patterns on the surface in a rhombic shape with a  $100\text{-}\mu\text{m}$  side. The groove width between two consecutive patterns was measured to be around  $25\ \mu\text{m}$ , indicating no overlapping between the patterns. The angle between fiber axis and helical pattern overtly validated the fabrication angle of  $45^\circ$ . Figure 13(b)

presents gross light distribution emitted from the diffuser tip with HeNe laser. Overall, photons were radially propagated along the optical diffuser without any significant of light delivery at the tip. It was observed that relatively higher intensity was accumulated near the proximal end of the diffuser.

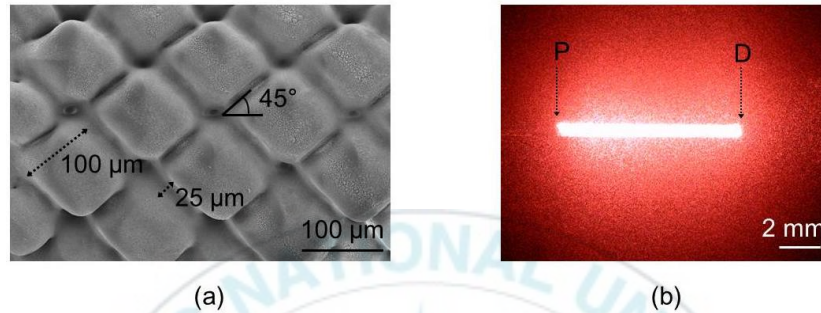


**Figure 13.** Images of optical diffuser fabricated at  $45^\circ$ . (a) SEM image (15 kV,  $\times 250$ ) of fiber surface. (b) HeNe light distribution from fiber tip (P: proximal and D: distal ends)

Various parameter sets of fabrication process were tested to find out the optimized one. In general, either higher fabrication power or longer interaction time between fiber surface and focused laser beam resulting in larger damage groove which may increase interface region with air (Fig. 14(b)). It might lead to enhancement of photon amount emitted in lateral direction as well as reduction photon amount in forward direction. However, high fabrication power could lead to increase in amount of photons emitted at the proximal end of the fiber resulting in a non-uniform light emission from the fiber tip.

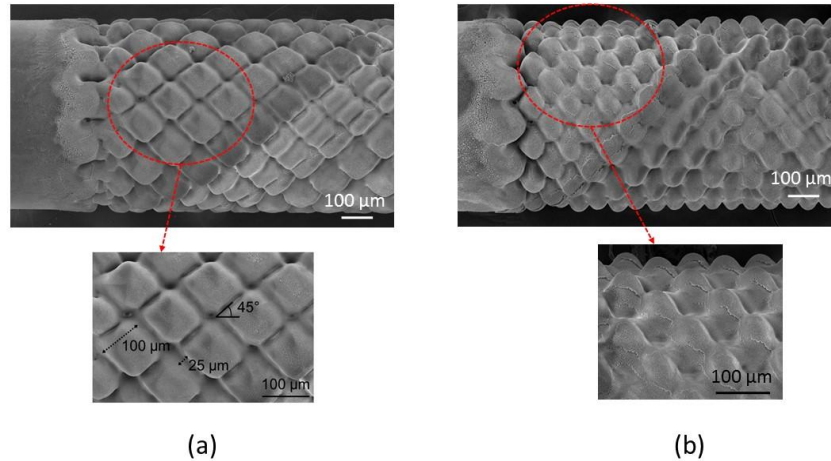


**Figure 14.** SEM images comparison between two diffusing fibers with different fabricated parameter. (a) 5 W CO<sub>2</sub> laser with short interaction time. (b) 6 W CO<sub>2</sub> laser with longer interaction time. Note that above images was  $\times 100$  magnification SEM and below image was

To improve the fabrication result in term of uniform emission from the diffuser tip as well as reduce light intensity emitted in forward direction, a tapering process was employed. Figure 14 presented a comparison in light intensity emitted in forward direction between with and without tapering process included by mean of azimuthal angle measurement. Tapered-based diffuser emits a 50% lower intensity in forward direction compared to a diffuser without tapering process employed.

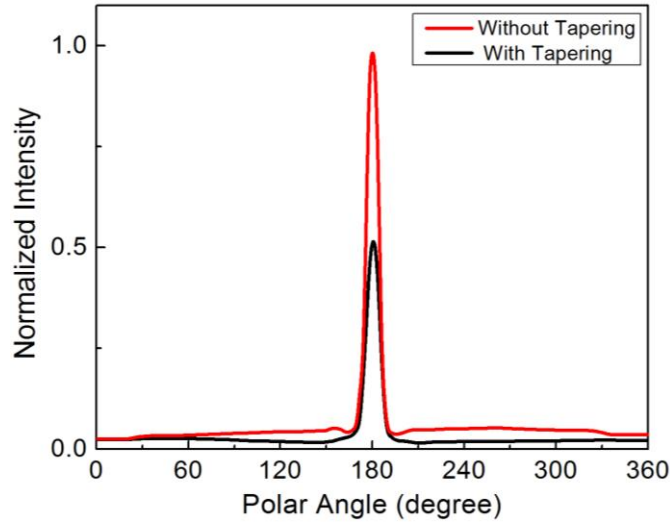


**Figure 15.** Demonstration of intensity comparison between two diffusing fiber: with and without tapering process

## 2. Spatial Emission from Diffuser tip

For quantitative evaluation on light diffusion, Fig. 16 exhibits spatial distribution of the normalized intensity from a diffuser tip in conjunction with HeNe. Polar emission results demonstrated almost isotropic radiation with less than 5% deviation from the average angular intensity over  $2\pi$  (i.e.,  $0.96 \pm 0.02$ ; Fig. 16(a)). The difference between the highest and lowest intensities was 8% (i.e.,  $0.92 \sim 1$ ). In addition, the irradiance distribution on a plane normal to the diffuser axis was associated with a concentric circle without any distortion, indicating homogenous and circumferential radiation from the diffuser tip. The overall shape shows two symmetric side-lobes at the angles of  $60^\circ$  and  $300^\circ$ , representing backward light diffusion. The lateral light distribution (i.e.,  $60 \sim 150^\circ$  and  $210 \sim 300^\circ$ ) also seemed rather uniform. The emission at the tip (i.e.,  $150 \sim 210^\circ$ ), however, revealed relatively lower

light intensity distribution. In Fig. 16(c), longitudinal emission demonstrated an asymmetric and less uniform profile of the light distribution from the optical diffuser. The highest intensity occurred near the proximal end of the diffuser, and the intensity immediately dropped at the location 3.5 *mm* away from the proximal end, which corresponded to the qualitative observation in Fig. 13(b). Then, the light intensity gradually increased along the diffuser tip toward the distal end. The difference between the highest and lowest intensities was estimated to be less than 25%.

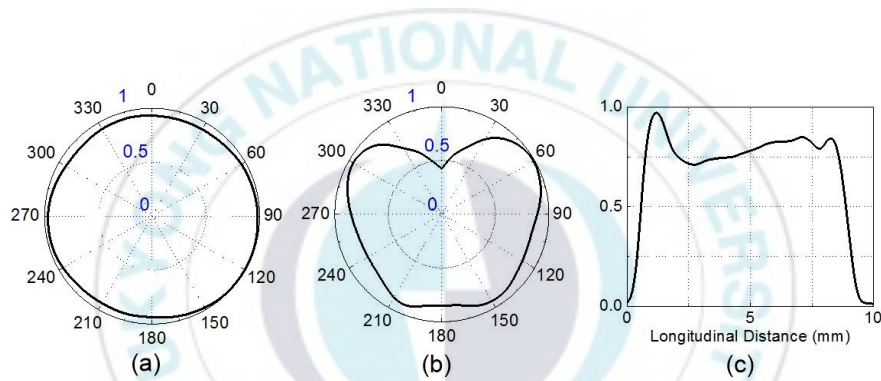


**Figure 16.** Normalized light intensity from 10 *mm* long diffusing fiber. (a) Polar emission. (b) Azimuthal emission. (c) Longitudinal emission

### 3. Simulation Results

Figure 17(a) demonstrates the temporal development of temperature at the glass-tissue interface under various power levels. Overall, the temperature rise increased with the applied power and irradiation time (Fig. 17(a)). As tissue coagulation occurs at the temperature ranging from 338 to 353 *K* [1], the

estimated increase rates to reach the coagulation point were 6, 11, and 16  $K/sec$  for 3, 6, and 9  $W$ , respectively.

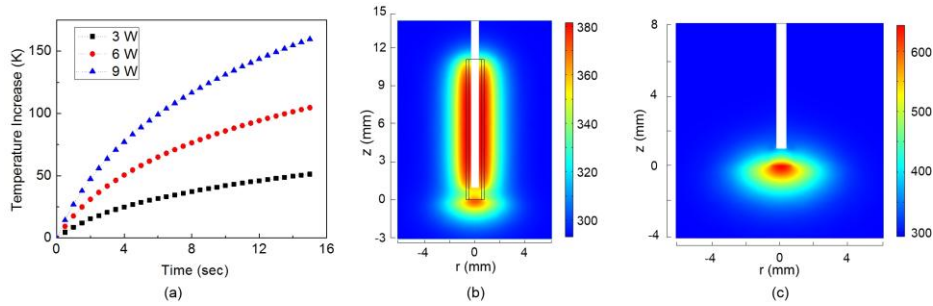


**Figure 17.** Spatial temperature distribution. (a) Temperature development at the tissue interface within 15  $sec$  irradiation time at three power levels: 3, 6, and 9  $W$ . (b) Longitudinal view of temperature distribution from diffuser tip after 10- $sec$ , 6  $W$ . (c) Longitudinal view of temperature distribution from flat-tip fiber after 10- $sec$ , 6  $W$

Figure 17(b) and Fig. 18(a) present the spatial distribution of tissue temperature irradiated at 6  $W$  for 10  $sec$ . The temperature was developed symmetrically around the diffuser axis. Due to a combination of forward and radial emissions, the fiber tip and the diffusing part yielded two different regions of heat distribution. Figure 17(b) exhibits the cross-sectional images of spatial temperature distribution along the diffuser (top) and perpendicular to the diffuser axis (bottom) after 6- $W$  irradiation for 10  $sec$ . Apparently, the different directions of light emissions resulted in two distinctive regions. Due to forward emissions, heat generation was diverged from the fiber tip in a conical shape. The peak temperature was found to be 365  $K$ , and then rapidly

decreased on account of beam divergence. On the other hand, radial emissions from the diffusing parts yielded almost symmetrical distribution in flat-top shape. The peak temperature at the interface between the glass-cap and the tissue was 380 K, which was slightly higher than that at the distal end.

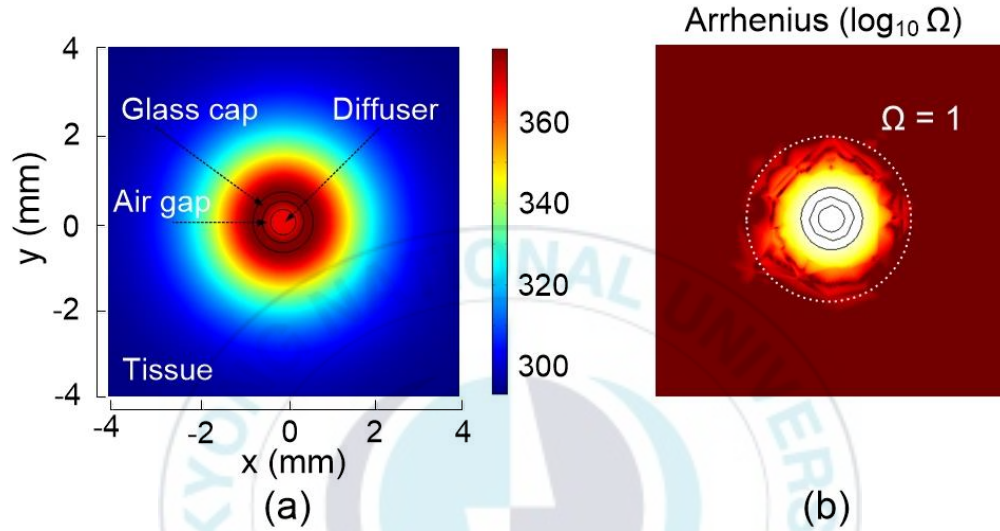


**Figure 18.** Thermal effect of 10-sec photocoagulation of diffuser. (a) Cross-sectional view of temperature distribution from diffuser tip. (b) Cross-sectional view of corresponding thermal damage with  $\log_{10}$  of Arrhenius integral

Figure 18(b) represents the extent of irreversible tissue damage ( $\Omega = 1$ ) corresponding to the temperature distribution in Fig. 18(a) in the diffuser-based model. The thermal denaturation was uniformly distributed along the diffuser and around the diffuser axis with coagulation thickness of  $1.3 \pm 0.2$  mm. In flat-tip fiber-based model, Fig. 19(a) represents temperature distribution while Fig 19(b) showed irreversible tissue damage accordingly.

The peak temperature was 650 K resulted from high intensity at the interaction point between laser beam and the tissue. It leads to totally damage to the tissue volume (Fig. 19(b)).

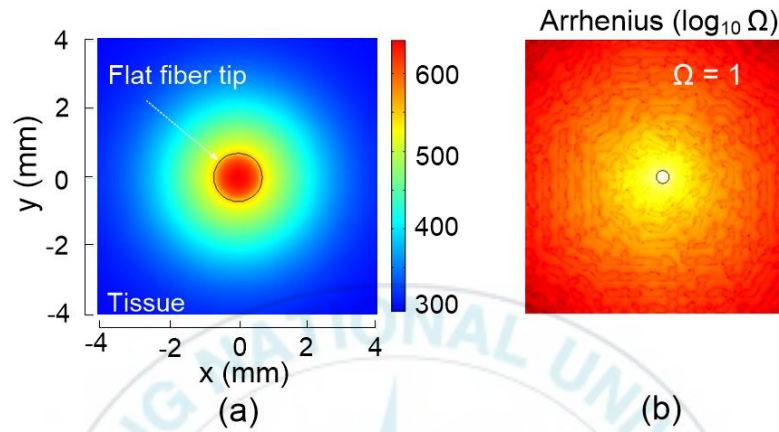


**Figure 19.** Thermal effect of 10-sec photocoagulation of flat-tip fiber. (a) Cross-sectional view of temperature distribution from incident region of laser beam. (b) Cross-sectional view of corresponding thermal damage with  $\log_{10}$  of Arrhenius integral

Figure 20 illustrates a comparison of spatial temperature distribution between flat-tip fiber and diffusing fiber in term of longitudinal and radial distance. In the case of flat-tip fiber, peak temperature was much higher than that in diffuser-based model (650 K compared to 380 K). The peak temperature in flat-tip fiber-based model obtained at the interaction region between laser beam and the tissue which was at the distance of 1 mm from the fiber end (Fig. 20(a)). In diffuser-based model, the peak temperature occurred

at tissue interface at the middle of diffuser tip (around 382 K) then the temperature was slightly decrease when it goes to two end of the diffuser tip. There is a significant drop in temperature at the region near the distal end of diffuser resulted in 1-*mm* air gap existed between distal end and the tissue due to low thermal conductivity of air (0.0257 W/m·K). For radial distance (Fig. 20(b)), both cases showed a same tendency in temperature decrease along radial distance resulted from thermal conductivity in tissue. Another reason was decrease in light intensity along tissue depth due to Beer's law. In general, diffusing fiber presented a uniform light emission with lower intensity compared to flat-tip fiber. It leads to much uniform thermal damage in a diffuser application compared to flat-tip fiber application.

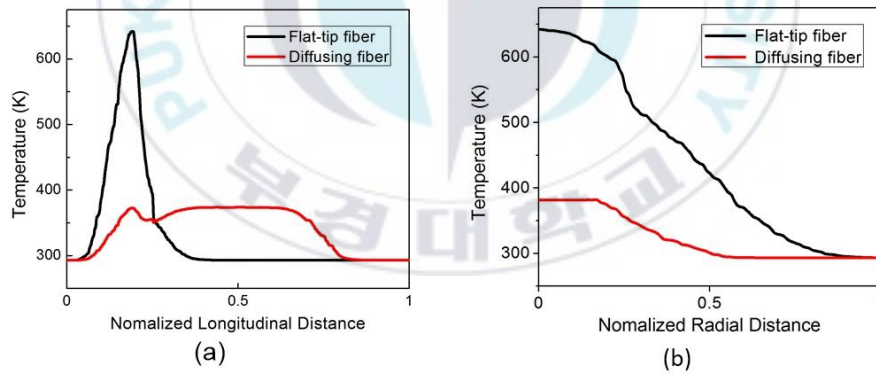


**Figure 20.** Spatial temperature distribution compared between flat-tip fiber and diffusing fiber in numerical simulation. (a) Along longitudinal distance. (b) In radial distance

An egg-white coagulation test was conducted to verify the performance of diffusing fiber. 5 W of 1470 nm laser was delivered by a diffusing fiber to

coagulate egg-white for 120 *sec* irradiation time. Figure 21(a) showed a glass-capped diffusing fiber before irradiation. A K-type thermal couple was used to measure the temperature increase during laser irradiation and a microscope was used to record and take images of denaturation process. The measurement point was at interface region between glass cap and the egg-white solution. Initial temperature of egg-white is around 288 *K*. After laser exposure, a coagulated egg-white formed of ellipsoid shape surrounding diffuser tip (Fig. 21(b)) was found. The coagulation in the egg-white was formed in an almost equivalent way to power distribution. Figure 21(c) illustrates temperature development at the egg-white interface as a function of irradiation time for three power level 2, 3, 4 *W*. Overall, the higher power resulted in the faster temperature increase. For 4 *W* application, the increase rate was around 2 *degree/sec*, and the temperature became saturated at 310 *K* in 40 *sec*, which corresponded to the temperature for thermal denaturation. Structure change in egg-white caused by heating from 293 *K* to 333 *K*, and egg-white has heat-caused denaturation caused by temperature above 314 *K*. Therefore there is nothing happened with 2 *W* power application. In the case of 3W power, a slow speed of denaturation change in egg-white resulted from a slow speed in temperature increase and low peak temperature (300 *K*).

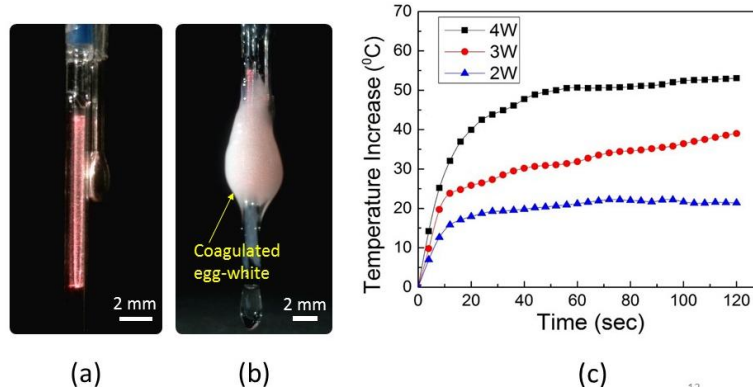


**Figure 21.** Egg-white coagulation test with 5-*W*, 1470-*nm* laser for 120-*sec* irradiation time. (a) Before irradiation. (b) After irradiation. And (c) Temperature development as a function of time at three power level 2, 3, and 4 *W*

#### 4. Tissue Test Results

Figure 22(a) exhibits spatio-temporal development of thermal denaturation at 6 *W* with a 45° fabricated diffuser in liver tissue. The onset of coagulation was found to be at 4 *sec* after laser irradiation. The most coagulated area in irregular shape occurred near the proximal end (i.e. top image of Fig. 22(a)) in an orthogonal direction from the fiber axis. Upon coagulation, the area of tissue coagulation apparently increased with irradiation time, eventually forming a narrow lopsided funnel shape of the denatured tissue (i.e. bottom image in Fig. 22(a)). With the identically fabricated diffusers, the effect of power on coagulation depth was also investigated in terms of irradiation time in Fig. 22(b). Overall, the depth linearly increased with both irradiation time and applied power ( $R^2 = 0.95\sim 0.99$ ). Higher power resulted in lower coagulation threshold (i.e. 1 *sec* at 9 *W* vs. 8 *sec* at 3 *W*), and the coagulation

rate was estimated to be 0.06, 0.08, and 0.10  $mm/sec$  at 3, 6, and 9  $W$  respectively.

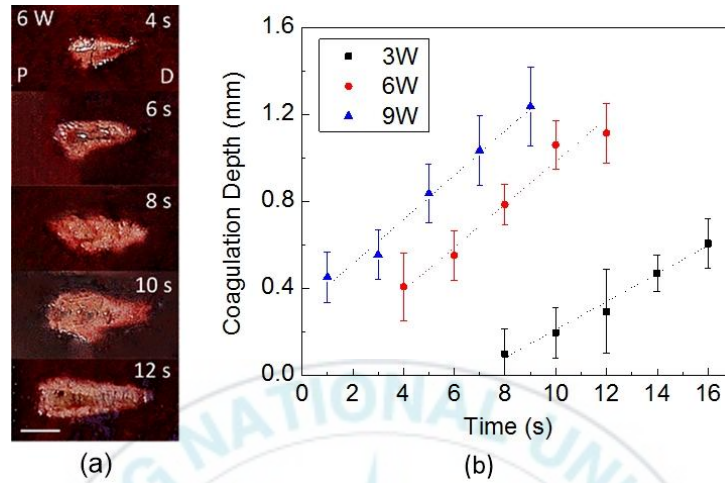


**Figure 22.** Effect of laser power on tissue coagulation with optical diffuser. (a) Temporal evolution of tissue coagulation at 6  $W$  with 1470  $nm$  (P: proximal and D: distal ends; bar = 5  $mm$ ). (b) Variations in coagulation depths as function of time for three different power levels ( $N = 5$ )

## 5. In Vitro Experiment Result

Figure 23 presents H&E-stained histology images of the urethral tissue treated at 6  $W$  for 10  $sec$ . The experimental conditions were selected to attain approximately 1  $mm$  of thermal denaturation in the tissue. According to the gross image (Fig. 23(a)), coagulative necrosis was vividly observed in the discolored, almost circumferential regions. The extent of coagulation thickness was measured to be  $1.3 \pm 0.2$   $mm$ , which was slightly thicker (18%) than liver testing under the same conditions (i.e.,  $1.1 \pm 0.1$   $mm$  in Fig. 22(b);

$p < 0.001$ ). The peripheral thermal damage was found owing to forward propagation of the laser light resulted from forward emission of laser light. Coagulative necrosis was clearly evidenced with the presence of epithelial cellular death, endothelial injury, formation of vacuolation, and infiltration of macrophages into the coagulated region. The preserved tissue still contained layers of smooth muscle cells without any cellular deformation, which is observed in a typical urethral tissue (Fig. 23(b)).

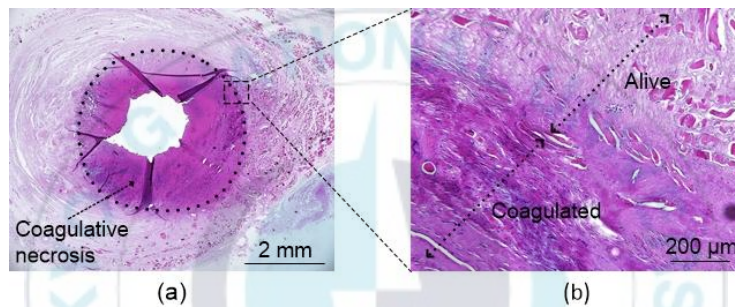


**Figure 23.** H&E-stained histological images of urethral tissue treated for 10 sec at 6 W with 1470 nm. (a) Gross image ( $\times 12.5$ ; bar = 2 mm). (b) Magnified image of transition zone ( $\times 100$ ; bar = 200  $\mu\text{m}$ )

#### IV. DISCUSSION

The goal of this study was to develop a novel optical fiber to deliver laser light radially to treat a cylindrical tissue such as urethra stricture. Laser-assisted micromachining was implemented to create periodic structural patterns on the fiber surface for light diffusion. For the sake of simplicity and reproducibility of fabrication process, helical groove patterns were selected and continuously engraved onto the surface of the fiber tip. The proposed fabrication typically requires less than five minutes creating the entire superficial deformation with the unvarying fiber diameter (i.e. cylindrical geometry rather conical). In turn, the current process was considerably faster and provided mechanically stronger samples than the previous other techniques [10, 11, and 23]. According to Figs. 16(a) and 16(c), both polar and longitudinal emission profiles quantitatively evidenced that the fabricated surface patterns (Fig. 13(a)) were able to more uniformly diffuse the transmitted light in a radial direction, compared with the previous diffusers [11, 23]. In addition, azimuthal emission indicated that less amount of the light (i.e., lower intensity) could be delivered in a forward direction, compared with conventional flat fibers. Accordingly, it is conceived that the proposed optical fiber could ensure favorable safety during endoscopic photothermal treatments (Figs. 17 and 18).

In spite of reproducible and circumferential tissue coagulation, experimental limitations still remain in photon distribution. For instance, azimuthal emissions presented that a certain amount of light was still transmitted in a forward direction (i.e., 150~210° in Fig. 16(b)), which could

be associated with safety issues during transurethral treatment. To further minimize the forward propagation, a conical tapering method is currently integrated into the fabrication process, in that a reduction in the cross-sectional diffuser area can lower the probability of the photons being transmitted through the tip. Another improvement is related to deletion of the abrupt intensity peak near the proximal end (Fig. 16(c)). According to microscopic evaluations, the observed discontinuity was associated with fabrication delays at the interface due the reverse change of machining directions. In turn, the protracted interaction time between laser and fiber surface led to formation of relatively deeper and wider holes near the proximal end, entailing more light diffusion. It is conceive that the application of concomitant light defocusing combined with high resolution stages can enhance the fabrication precision as well as reduce the machining time particularly at the boundary. Moreover, the current fabrication process merely implemented the fixed machining parameters (i.e.,  $45^\circ$  pattern,  $100\ \mu\text{m}$  in segment size, and  $25\ \mu\text{m}$  gap in Fig. 13(a)). Since flat-top lateral emission is the eventual goal of the fiber machining, further dosimetric investigations will be performed to optimize a variety of fabrication parameters including patterning angle, groove width, and segment size. Various coating materials can also be applied to the glass cap not only to protect the fiber tip from mechanical shock and but also facilitate the light diffusion at the cap surface.

According to numerical simulations (Fig. 17(b)), spatial distributions of temperature largely reflected a comparable shape of tissue coagulation (Fig. 7(a)), where the tissue temperature experienced around  $338\ \text{K}$  or higher [1].

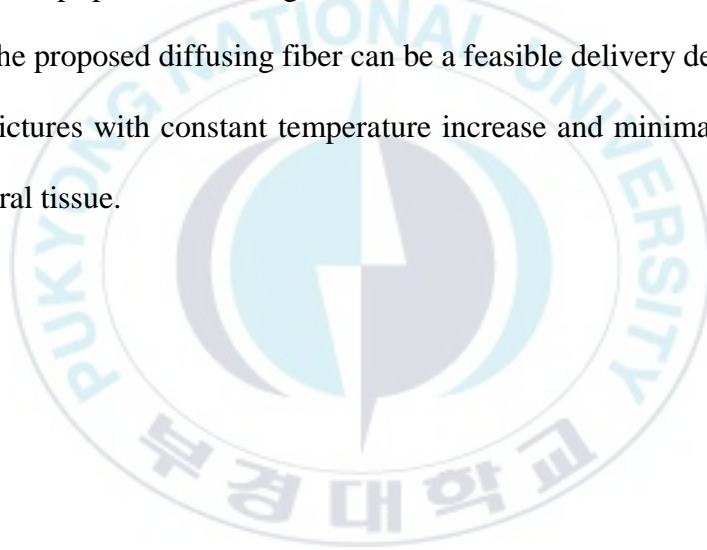
However, due to 20% of laser power emitting in a forward direction, the temperature at the distal end was distributed rather hemi-spherically (Fig. 5(b)) whereas the in vitro testing demonstrated a funnel shape of tissue coagulation (Fig. 23(a)). The discrepancy could have been in association with increased specular reflection at the glass-tissue interface and augmented scattering during tissue denaturation [18, 20]. In turn, less amount of light might be able to propagate in a forward direction as the coagulation process advanced. Furthermore, the simulation model yielded the overall coagulation depth approximately 20% thicker than the tissue testing at 6 W for 10-sec irradiation (i.e.,  $1.3 \pm 0.2$  mm for simulation vs.  $1.1 \pm 0.2$  mm for tissue testing). The thinner coagulation depth in the liver tissue could result from output power fluctuations and less homogeneous intensity distribution during interstitial photocoagulation. Another explanation for the difference could be pertaining to the empirical values of  $A_f$  and  $E_a$  as well as dynamic effects of tissue properties (optical and thermal), which could affect thermal sensitivity in tissue during the coagulation. Thus, incorporation of refined power regulation and dynamic thermal responses of tissue will improve computation accuracy as well as specifically predict the extent of thermal necrosis in the tissue. Urethra tissue testing confirmed almost circular shape of coagulative necrosis (Fig. 23(a)), which shows a good agreement with the degree of irreversible damage in Fig. 18(b). Unlike the liver testing, almost equivalent thermal coagulation ( $p = 0.99$ ) was found between the numerical model and the urethral tissue, which could be attributed to slightly higher light absorption characteristics of urethral tissue at 1470 nm ( $\mu_{a,urethra} = 22.5 \text{ cm}^{-1} = 90\%$  of

interstitial water  $\times 25 \text{ cm}^{-1}$  [21, 22]) than liver ( $\mu_{a,liver} = 19 \text{ cm}^{-1}$ ) along with comparable thermal diffusivity ( $\alpha_{urethra} = 1.34 \times 10^{-4} \text{ mm}^2/\text{s}$  vs.  $\alpha_{liver} = 1.36 \times 10^{-4} \text{ mm}^2/\text{s}$ ).

In vitro results demonstrated a slightly asymmetric coagulation (i.e., thicker at 5 o'clock) in urethra with the eccentricity of 0.3 mm despite that the urethral wall was circumferentially coagulated (Fig. 23(a)). An explanation for the out-of-center phenomenon could be blind deployment of an optical diffuser during the test. Since the inner structure of the tissue was irregular, the diffuser was difficult to precisely locate at the center of the urethra for securing consistent thermal denaturation. In fact, the end-point of laser stricture treatment is to extend the narrowed urethral pathway for easy urination without development of inflammation or infection. Hence, the integration of an inflatable stent or catheter into the proposed diffuser is currently under consideration to deploy the transurethral device in a reliable and concentric manner. The dilation of the device with increasing diameters can also apply mechanical pressure in a radial direction to the urethral wall and conceivably induce structural deformation during the irradiation. Furthermore, in vivo experiments using a mini-pig model [23] will be conducted to identify acute and chronic responses of the treated tissue. The feasibility of achieving the complete stricture removal in should thus be evaluated terms of various disease geometries and therapeutic parameters including diffuser length, wavelength, pulse configurations, and irradiance.

## V. CONCLUSION

The current study demonstrated a simple and effective method to fabricate a diffusing optical fiber with helical patterns. Due to periodic surface deformation, the diffuser could deliver laser light circumferentially with unvarying low intensity, compared to flat fibers. The cylindrical light diffusion could also achieve a conical shape of tissue coagulation, implicating a viable way of inducing photothermal interactions to treat tubular urethral tissues. Further developments on fabrication technique will be pursued to entail a flat-top profile of longitudinal emissions in a more predictable manner. The proposed diffusing fiber can be a feasible delivery device to treat urethral strictures with constant temperature increase and minimal damage to the peripheral tissue.



## VI. FUTHER STUDIES

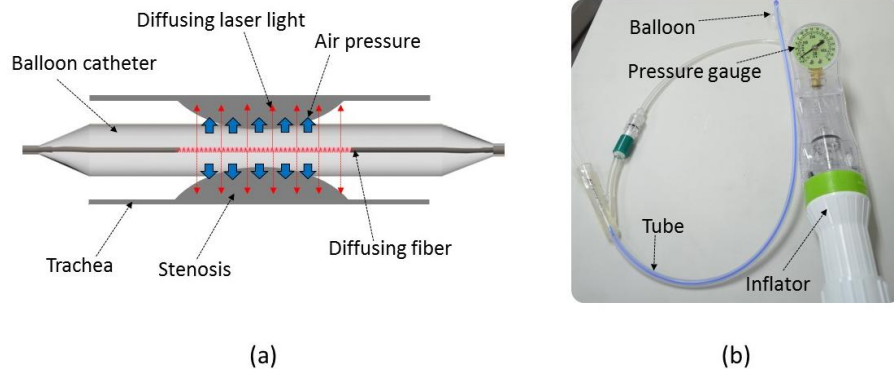


**Figure 24.** Balloon catheter-based diffusing fiber. (a) Principle of the combined technique between balloon and diffuser. (b) Real image of the device including an inflator

For the future study, a diffuser can be a feasible tool applied for treat another tubular tissue structure. That is tracheal stenosis. Since trachea has a quite bigger in diameter ( $\sim 20\text{ mm}$ ) compared to urethra ( $\sim 1.5\text{ mm}$ ), a balloon catheter will be employed to enhance efficacy of the treatment. Integrating an optical diffuser with a balloon catheter might a feasible technique which gives a combination of mechanical pressure and thermal effect. Therefore, the combined treatment can achieve a permanent change in tissue structure and also extend coverage of treatment. From Fig. 24(a), the role of balloon application to apply mechanical pressure to tracheal wall for extension during laser treatment. Figure 24(b) shows how a balloon catheter-based diffuser look like. The balloon was made by silicon which is transparent of laser light and also flexible to inflate.

We are working on the tracheal stenosis treatment with balloon catheter-based diffuser. A histology for acute and chronic in vivo experiments was also conducted to see how healing response progresses.

For the safely purpose, all physical signals from the treatment process should be monitored. In order to maintain the temperature during the treatment, a real time temperature feedback controller will be employed. In general, a standard feedback controller includes a standard PID controller, temperature sensor in conjunction with temperature transmitter and a manipulated actuator. In this study, temperature sensor is a wide range K-type thermocouple. On other hand, the manipulated actuator is obviously laser system. The error signal between desired and actual temperature will be calculated as the input signal for the controller. Based on this input value, the controller will give an appropriate control signal to the laser system. Thus, the treatment temperature will be maintained at stable value during the treatment. For pressure monitoring, a pressure sensor in conjunction with a pressure transmitter was applied to measure the air pressure during inflating step.

## References

1. B. Cox, "Introduction to laser-tissue interactions," *PHAS* **4886**, 1-61 (2007).
2. C. Chapple, D. Andrich, A. Atala, G. Barbagli, A. Cavalcanti, S. Kulkarni, A. Mangera, and Y. Nakajima, "SIU/ICUD Consultation on Urethral Strictures: The management of anterior urethral stricture disease using substitution urethroplasty," *Urology* **83**, S31-47 (2014).
3. R. A. Santucci, G. F. Joyce, and M. Wise, "Male urethral stricture disease," *J Urol* **177**, 1667-1674 (2007).
4. A. Mangera and C. R. Chapple, "Urethral stricture disease," *Surgery (Oxford)* **32**, 304-309 (2014).
5. R. Mathur, D. Nayak, G. Aggarwal, A. Shukla, F. Khan, and S. Odiya, "A Retrospective Analysis of Urethral Strictures and Their Management at a Tertiary Care Center," *Nephro Urol Mon* **3**, 109-113 (2011).
6. M. Amzayyb, R. R. van den Bos, V. M. Kodach, D. M. de Bruin, T. Nijsten, H. A. Neumann, and M. J. van Gemert, "Carbonized blood deposited on fibres during 810, 940 and 1,470 nm endovenous laser ablation: thickness and absorption by optical coherence tomography," *Lasers in medical science* **25**, 439-447 (2010).
7. H. W. Kang, J. Kim, and J. Oh, "Enhanced photocoagulation with catheter-based diffusing optical device," *Journal of biomedical optics* **17**, 118001 (2012).
8. R. G. Kolkman, W. Steenbergen, and T. G. van Leeuwen, "In vivo photoacoustic imaging of blood vessels with a pulsed laser diode," *Lasers in medical science* **21**, 134-139 (2006).
9. K. Miyazaki, Y. Morimoto, N. Nishiyama, Y. Maekawa, W. Z. Hu, K. Nakatate, K. Kaneda, N. Shinomiya, and K. Kataoka, "A novel homogeneous irradiation fiber probe for whole bladder wall photodynamic therapy," *Lasers Surg Med* **44**, 413-420 (2012).
10. R. K. Singal, J. D. Denstedt, H. A. Razvi, and S. S. Chun, "Holmium:YAG laser endoureterotomy for treatment of ureteral stricture," *Urology* **50**, 875-880 (1997).
11. K. Hashimoto, M. Kogure, T. L. Irwin, K. Tezuka, T. Osawa, K. Kato, and T. Ebisawa, "Permanent hair removal with a diode-pumped Nd:YAG laser: a pilot study using the direct insertion method," *Journal of the American Academy of Dermatology* **49**, 1071-1080 (2003).
12. M. A. Kosoglu, R. L. Hood, J. H. Rossmeisl, D. C. Grant, Y. Xu, J. L. Robertson, M. N. Rylander, and C. G. Rylander, "Erratum: Fiberoptic microneedles: Novel optical diffusers for interstitial delivery of therapeutic light," *Lasers in Surgery and Medicine* **43**, 1008-1014 (2011).

13. M. A. Kosoglu, R. L. Hood, Y. Chen, Y. Xu, M. N. Rylander, and C. G. Rylander, "Fiber optic microneedles for transdermal light delivery: ex vivo porcine skin penetration experiments," *Journal of biomechanical engineering* **132**, 091014 (2010).
14. V. V. Volkov, V. B. Loshchenov, V. I. Konov, and V. V. Kononenko, "Fibreoptic diffuse-light irradiators of biological tissues," *Quantum Electronics* **40**, 746 (2010).
15. L. M. Vesselov, W. Whittington, and L. Lilge, "Performance evaluation of cylindrical fiber optic light diffusers for biomedical applications," *Lasers Surg Med* **34**, 348-351 (2004).
16. J. Kwon, C. Y. Lee, J. Oh, and H. W. Kang, "Computational analysis of endometrial photocoagulation with diffusing optical device," *Biomedical optics express* **4**, 2450-2462 (2013).
17. G. V. G. Baranoski and J. G. Rokne, "An Algorithmic Reflectance and Transmittance Model for Plant Tissue," *Computer Graphics Forum* **16**, C141-C150 (1997).
18. J. P. Ritz, A. Roggan, C. Isbert, G. Muller, H. J. Buhr, and C. T. Germer, "Optical properties of native and coagulated porcine liver tissue between 400 and 2400 nm," *Lasers Surg Med* **29**, 205-212 (2001).
19. K. J. Bergemann, R. Krasny, and S. R. Forrest, "Thermal properties of organic light-emitting diodes," *Organic Electronics* **13**, 1565-1568 (2012).
20. A. N. Bashkatov, E. A. Genina, V. I. Kochubey, A. A. Gavrilova, S. V. Kapralov, V. A. Grishaev, and V. V. Tuchin, "Optical properties of human stomach mucosa in the spectral range from 400 to 2000 nm: Prognosis for gastroenterology," *Medical Laser Application* **22**, 95-104 (2007).
21. S. L. Jacques, "Optical properties of biological tissues: a review," *Phys Med Biol* **58**, R37-61 (2013).
22. R. R. van den Bos, P. W. van Ruijven, C. W. van der Geld, M. J. van Gemert, H. A. Neumann, and T. Nijsten, "Endovenous simulated laser experiments at 940 nm and 1470 nm suggest wavelength-independent temperature profiles," *European journal of vascular and endovascular surgery : the official journal of the European Society for Vascular Surgery* **44**, 77-81 (2012).
23. K. D. Sievert, C. Selent-Stier, J. Wiedemann, T. O. Greiner, B. Amend, A. Stenzl, G. Feil, and J. Seibold, "Introducing a large animal model to create urethral stricture similar to human stricture disease: a comparative experimental microscopic study," *J Urol* **187**, 1101-1109 (2012).

## **Acknowledgments**

I would like to thank H. Shin for his help on tissue testing and M. Ahn for tissue preparation.

I would like to thank Hoang-Phuoc Ho, Thanh-Canh Huynh, 황지은, 김한나, Yu Gyeong Chae and Kyu Kyu Hlaing, who as good friends, was always give me best suggestions and kindly mobilization. Special thanks to Dr. Jung Hwan Oh and Dr. Seung Yun Nam, who were willing to participate in my final defense committee.

I would like to gratefully and sincerely thank author's advisor-Dr. Hyun Wook Kang for his excellent guidance, patience and providing me with good foundation and knowledge during Master course at the Bio-Ablation Laboratory, Biomedical Engineering Department, Pukyong National University.

Finally, I would like to thank my parents who were always supporting me and encouraging me with their best wishes.

This research was supported by Basic Science Research Program through the National Research Foundation of Korea (NRF) funded by the Ministry of Education, Science and Technology (NRF-2014R1A1A2060112).